
[View Journal Online](#)
[View Article Online](#)

Synthesis, crystal structure, and electrochemical hydrogenation of the $\text{La}_2\text{Mg}_{17-x}\text{M}_x$ ($M = \text{Ni}, \text{Sn}, \text{Sb}$) solid solutions

Vasyl Kordan ^{1,*}, Vitalii Nytko ¹, Ivan Tarasiuk ¹, Oksana Zelinska ¹ and Volodymyr Pavlyuk ^{1,2}

¹ Department of Inorganic Chemistry, Faculty of Chemistry, Ivan Franko National University of Lviv, Kyryla i Mefodiya St., 6, 79005 Lviv, Ukraine
kordan50@gmail.com (V.K.), vetalnitka@gmail.com (V.N.), tarasiuk.i@gmail.com (I.T.), oksana.zelinska@gmail.com (O.Z.), vpavlyuk2002@yahoo.com (V.P.)

² Institute of Chemistry, Jan Długosz University of Częstochowa, Armii Krajowej Ave, 13/15, 42200, Częstochowa, Poland

* Corresponding author at: Department of Inorganic Chemistry, Faculty of Chemistry, Ivan Franko National University of Lviv, Kyryla i Mefodiya St., 6, 79005 Lviv, Ukraine.

e-mail: vasyl.kordan@lnu.edu.ua (V. Kordan).

RESEARCH ARTICLE

ABSTRACT



 10.5155/eurjchem.12.2.197-203.2092

Received: 30 January 2021

Received in revised form: 24 March 2021

Accepted: 31 March 2021

Published online: 30 June 2021

Printed: 30 June 2021

KEYWORDS

Hydrides
 Hydrogenation
 Electrochemistry
 Intermetallic phases
 Electron microscopy
 Single crystal structure

The crystal structure of $\text{La}_2\text{Mg}_{17-x}\text{Sn}_x$ solid solution was determined by single crystal X-ray diffraction for the first time. This phase crystallizes in hexagonal symmetry with space group $P6_3/mmc$ ($a = 10.3911(3)$, $c = 10.2702(3)$ Å, $V = 960.36(6)$ Å³, $R_1 = 0.0180$, $wR_2 = 0.0443$ for the composition $\text{La}_{3.65}\text{Mg}_{30}\text{Sn}_{1.10}$) and is related to the structure of $\text{CeMg}_{10.3}$ and $\text{Th}_2\text{Ni}_{17}$ -types which are derivative from the CaCu_5 -type. A series of isotypical solid solutions $\text{La}_2\text{Mg}_{17-x}\text{M}_x$ ($M = \text{Ni}, \text{Sn}, \text{Sb}$, $x \sim 0.8$) was synthesized and studied by X-ray powder diffraction, energy dispersive X-ray spectroscopy and fluorescent X-ray spectroscopy. All solid solutions crystallize with the structure related to the $\text{Th}_2\text{Ni}_{17}$ -type. The electrochemical hydrogenation confirmed the similar electrochemical behavior of all studied alloys. The amount of deintercalated hydrogen depends on the physical and chemical characteristics of doping elements and increases in the sequence $\text{Sn} < \text{Mg} < \text{Sb} < \text{Ni}$. The most geometrically advantageous sites are octahedral voids $6h$ of the initial structure, thus a coordination polyhedron for H-atom is an octahedron $[\text{HLa}_2(\text{Mg},\text{M})_4]$.

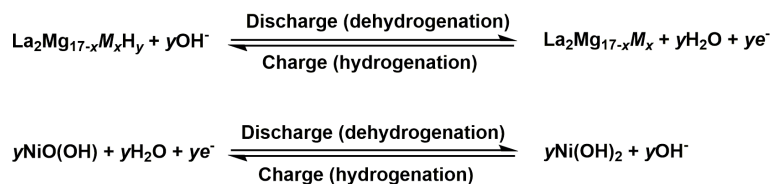
Cite this: *Eur. J. Chem.* 2021, 12(2), 197-203

Journal website: www.eurjchem.com

1. Introduction

Nowadays, materials related to the production, storage and conversion of energy are in great demand in different fields of technology and industry. The most profitable energy storage is possible during the accumulation of charge in various batteries or storage stations. Most of the batteries use intermetallic phases or composites with metallic matrix as electrodes [1]. Phases with large voids, such as R_5M_3 (Mn_5Si_3 -type structure), are suitable for Li or Mg intercalation and can be promising electrode materials for corresponding Li-ion and Mg-ion batteries [2-5]. In the era of the development of alternative energy sources, the modern research works are associated with the study of the hydrogenation of alloys, which can be used for hydrogen storage purposes and as electrode materials for nickel metal hydride batteries. Materials with the best hydrogen absorption properties were developed on the basis of the structure types CaCu_5 , MgCu_2 , MgZn_2 , MgNi_2 , CeNi_3 , Gd_2Co_7 , ZrNiAl , Mo_2FeB_2 , $\text{Th}_2\text{Zn}_{17}$, $\text{Th}_2\text{Ni}_{17}$ and their derivatives. Doping of metals and alloys by *s*- or *p*-elements positively influence on the electrochemical and sorption properties of the samples of

electrodes. For instance, doping of magnesium by Li and Al improves its hydrogen sorption and corrosion resistance [6,7], doping of $\text{Tb}_2\text{Ni}_{17}$ by Li, Mg, Al, Ge, Sn, Sb and Bi also enhances its corrosion resistance and discharge time of the battery [8]. The alloys containing Mg became popular for the development of light and safe for the environment materials. As a basis are the phases that crystallize in the structure type CaCu_5 or its derivatives [9-15]. Gas hydrogenation and optimization of the synthesis procedure of the composite based on the mixture of $\text{La}_2\text{Mg}_{17}$ and LaNi_5 is presented in Ref. [16]. In this case, LaNi_5 accelerates the hydrogen sorption and desorption processes. The solubility of Sn in the $\text{La}_2\text{Mg}_{17}$ phase does not exceed 2 at. % at 500 °C according to Ref. [17], while in our research the solubility reaches 4 at. % at 400 °C that is confirmed by X-ray powder diffraction (XRD) and energy dispersive X-ray spectroscopy (EDX). The purpose of this research is to study the crystal structure of $\text{La}_2\text{Mg}_{17-x}\text{M}_x$ solid solutions and find the correlation between composition of the electrodes and their electrochemical characterization during hydrogenation/dehydrogenation processes.



Scheme 1

2. Experimental

2.1. Synthesis of samples

Lanthanum, tin, antimony, nickel (commercial, small pieces), and magnesium (commercial powder) with nominal purity > 99.9 wt. % were used as starting materials. Similar method of synthesis is described in [5]. Alloys with the composition $\text{La}_{10.5}\text{Mg}_{85.5}\text{M}_4$, ($M = \text{Ni}, \text{Sn}, \text{Sb}$) were prepared by induction melting (re-melted two times) of pressed pellets of pure components (excess of Mg was 5 wt. % and Sb was 2 wt. %) under the purified argon atmosphere. To reach homogeneity the samples were sealed in evacuated silica tubes, annealed at 400 °C for 2 months and finally quenched in cold water. During the synthesis, the lost of weight did not exceed 2 wt. %. Higher annealing temperature, for example 600 °C causes the interaction of magnesium with surface of silica tube and further component loss.

2.2. Phase analysis

The phase analysis of the alloys before electrochemical processes was mainly carried out by powder X-ray diffraction using a diffractometer DRON-2.0M ($\text{FeK}\alpha$ -radiation, $\lambda = 1.93608 \text{ \AA}$, $20^\circ \leq 2\theta \leq 100^\circ$). The refinement of lattice parameters (least squares refinement method) was performed using LATCON [18] and PowderCell [19] programs.

Qualitative and quantitative composition of the observed phases was studied using scanning electron microscope TESCAN Vega3 LMU (Oxford Instruments energy dispersive X-ray analyzer, Aztec ONE system) and REMMA-102-02. X-ray fluorescent spectroscopy (spectrometer ElvaX Pro) was used for investigation of the integral composition of electrodes before and after hydrogenation.

2.3. Electrochemical measurements

Electrochemical hydrogenation of a binary $\text{La}_2\text{Mg}_{17}$ and three ternaries (doped by 4 at. % of Ni, Sn, and Sb) alloys was carried out in 2-electrode Swagelok-type cells. The battery prototype consisted of a negative electrode containing 0.3 g of the studied alloy and a positive electrode containing a mixture of dried $\text{Ni}(\text{OH})_2$ (mixture of α - and β -modifications) with 10 wt. % of graphite. A separator soaked in 6M KOH electrolyte (prepared from KOH with 99 wt. % purity, commercial) was placed between the electrodes to avoid contact. Chronopotentiograms of the Ni-MH battery prototypes were obtained in galvanostatic regime over 50 cycles using galvanostat MTECH G410-2 [20]. The amount of deintercalated H-atoms per formula unit (H/f.u.) was determined for studied electrodes using Faraday's formula, where H-content is directly proportional to the discharge time and inversely proportional to the amount of electrode material. The electrochemical reactions that occur on the electrodes can be presented by Scheme 1.

2.4. Single crystal determination

The crystal structure of the $\text{La}_2\text{Mg}_{17-x}\text{Sn}_x$ solid solution was studied by single crystal X-ray diffraction (diffractometer

Xcalibur Oxford Diffraction, CCD-detector, $\text{Mo K}\alpha_1$ -radiation, ω -scan mode). A single crystal for investigation was selected from the alloy with the composition $\text{La}_{10.5}\text{Mg}_{85.5}\text{Sn}_4$. Absorption correction was performed by an empirical method using SADABS [21]. The analysis of the crystal structure was carried out by direct method using SHELXS [22] and full matrix least squares refinement on F^2 was performed using SHELXL [23].

3. Results and discussion

3.1. Crystal structure of the $\text{La}_{3.65}\text{Mg}_{30}\text{Sn}_{1.10}$

During the systematic investigation of the interaction between metallic components in the systems La-Mg-Sn, Sb , we observed the formation of the solid solutions of substitution on the basis of the binary phase $\text{La}_2\text{Mg}_{17}$ (ordered model with structure type $\text{Th}_2\text{Ni}_{17}$, space group $P6_3/mmc$, Pearson's code $hP38$, $Z = 2$) with the homogeneity range up to 4 at.% of Sn or Sb. This structure is suitable for hydrogen storage and the phases with the same or relative crystal structure can serve as a negative electrode material in Ni-MH batteries. Detailed study of the crystal structure of this solid solution was carried out by single crystal X-ray powder diffraction on the sample $\text{La}_{10.5}\text{Mg}_{85.5}\text{Sn}_4$, from which an irregularly shaped single crystal was selected. Solution the structure by direct methods indicated a significant disorder of the structure and the presence of split positions for La_2Sn_2 and Sn_1Sn_3 . The refined composition from X-ray data is $\text{La}_{3.65}\text{Mg}_{30}\text{Sn}_{1.10}$. The crystal data and details of the structure refinement for $\text{La}_{3.65}\text{Mg}_{30}\text{Sn}_{1.10}$ are given in Table 1. The standardized atomic positions and thermal displacement parameters are given in Table 2.

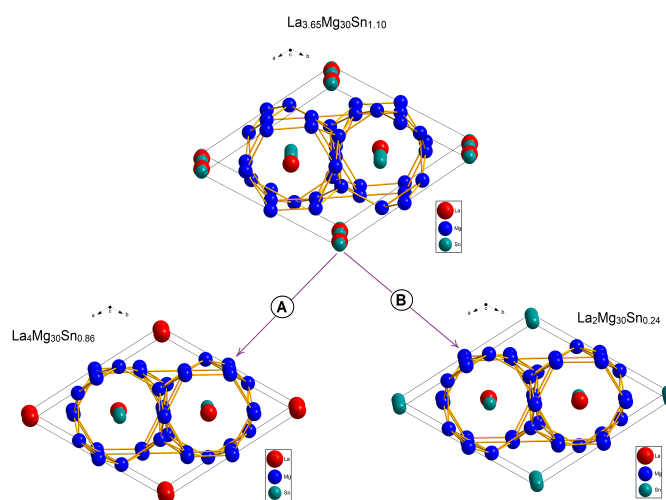
The results of structural refinement show that the formation of a $\text{La}_2\text{Mg}_{17-x}\text{Sn}_x$ solid solution takes place by a complex mechanism. If the binary phase $\text{La}_2\text{Mg}_{17}$ dissolves tin, the Mg-atoms are replaced by Sn-atoms in a site 4f and additional Sn-atoms are inserted in the positions 4e and 2d, which are empty in the initial binary structure. The insertion of Sn atoms in the site 2b causes the subtraction of La atoms from 2b site because La_2Sn_2 are in the split position. It proves that $\text{La}_{3.65}\text{Mg}_{30}\text{Sn}_{1.10}$ is more closely related to $\text{CeMg}_{10.3}$ -type (disordered model) [24], however, it also differs from it due to the redistribution of atoms at some sites. (Table 3). The $\text{La}_{3.65}\text{Mg}_{30}\text{Sn}_{1.10}$ structure is strongly disordered, as evidenced by the presence of adjacent atomic sites, which can not be occupied simultaneously, and by the existence of split positions. Therefore, in the average structure, two subcells (A and B) can be selected, with the fraction ratio of subcell A to subcell B as 4:1 (Figure 1). The A subcell has a composition $\text{La}_4\text{Mg}_{30}\text{Sn}_{0.86}$ and B subcell has a composition $\text{La}_2\text{Mg}_{30}\text{Sn}_{0.24}$. Detailed crystal chemical analysis shows that La1 and La2 atoms are enclosed in a pseudo-Frank-Kasper polyhedra [$\text{La}_1\text{Mg}_{18}\text{Sn}_{20}$] and [$\text{La}_2\text{Mg}_{18}$] respectively. For all Mg and Sn3 atoms typical is icosahedral coordination. The Sn1 and Sn2 atoms are enclosed in 14-vertex polyhedra [$\text{Sn}_1\text{Mg}_{12}\text{SnLa}$] and [$\text{Sn}_2\text{Mg}_{12}\text{Sn}_2$] that can be treated as bicapped hexagonal antiprisms. The unit cell and coordination polyhedra of atoms are shown in Figure 2.

Table 1. Crystal data and details of the structure refinement for $\text{La}_{3.65}\text{Mg}_{30}\text{Sn}_{1.10}$.

Parameters	Compound
Empirical formula	$\text{La}_{3.65}\text{Mg}_{30}\text{Sn}_{1.10}$
Formula weight (g/mol)	1366.7
Temperature (K)	298
Crystal system	Hexagonal
Space group	$P6_3/mmc$
a, (Å)	10.3911(3)
b, (Å)	10.3911(3)
c, (Å)	10.2702(3)
Volume (Å ³)	960.36(6)
Z	1
ρ_{calc} (g/cm ³)	2.363
μ (mm ⁻¹)	5.17
F(000)	623
Crystal size (mm ³)	0.06 × 0.06 × 0.02
Radiation	MoK α ($\lambda = 0.71073$)
2 θ range for data collection (°)	2.3 to 26.3
Index ranges	-12 ≤ h ≤ 12, -12 ≤ k ≤ 12, -12 ≤ l ≤ 12
Reflections collected	8711
Independent reflections	408 [R _{int} = 0.0261]
No. of reflections with I > 2 σ (I)	339
Data/parameters	408/28
Goodness-of-fit on F ²	1.27
Final R indexes [I ≥ 2 σ (I)]	R ₁ = 0.0180 wR ₂ = 0.0443
Final R indexes [all data]	R ₁ = 0.0241, wR ₂ = 0.0498
Largest diff. peak/hole (e Å ⁻³)	0.34/-0.86

Table 2. Fractional atomic coordinates and thermal displacement parameters (Å²) for $\text{La}_{3.65}\text{Mg}_{30}\text{Sn}_{1.10}$.

Atoms	Wyckoff sites	x	y	z	$U_{\text{iso}}/U_{\text{eq}}$	Occ. (<1)
La1	2c	1/3	2/3	1/4	0.01499(18)	
La2	2b	0	0	1/4	0.0183(2)	0.827(3)
Mg1	12k	0.36045(16)	0.03294(16)	1/4	0.0246(3)	
Mg2	12j	0.16402(7)	0.32803(14)	0.02035(13)	0.0221(3)	
Mg3	6g	1/2	0	0	0.0195(4)	
Sn1	4f	1/3	2/3	0.6018(2)	0.025	0.2174(15)
Sn2	4e	0	0	0.1015(12)	0.027	0.0404(12)
Sn3	2d	1/3	2/3	3/4	0.027	0.032(2)
Atoms	U^{11}	U^{22}	U^{33}	U^{12}	U^{13}	U^{23}
La1	0.0151(2)	0.0151(2)	0.0147(3)	0.00757(11)	0.000	0.000
La2	0.0165(2)	0.0165(2)	0.0220(4)	0.00824(12)	0.000	0.000
Mg1	0.0395(8)	0.0261(7)	0.0159(6)	0.0222(6)	0.000	0.000
Mg2	0.0164(5)	0.0253(7)	0.0277(6)	0.0126(3)	0.0012(3)	0.0024(6)
Mg3	0.0156(6)	0.0236(9)	0.0220(8)	0.0118(4)	-0.0005(4)	-0.0010(8)

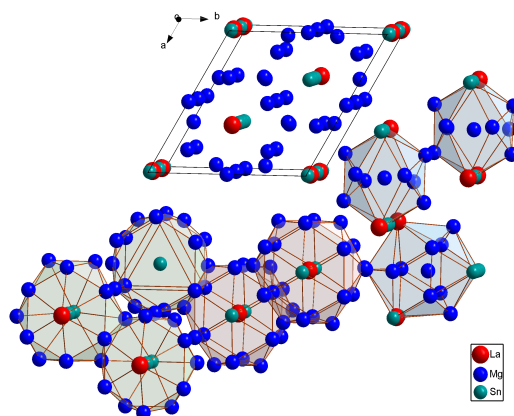
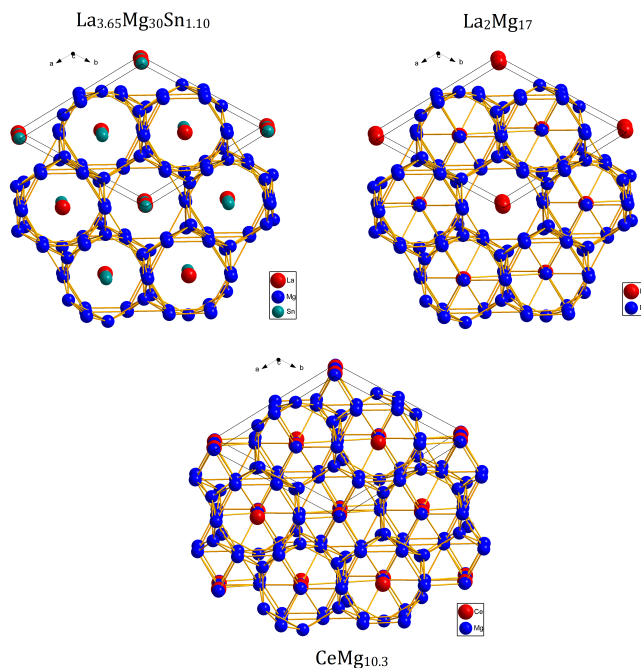
**Figure 1.** $\text{La}_{3.65}\text{Mg}_{30}\text{Sn}_{1.10}$ as a composite structure of A and B subcells.

The $\text{La}_{3.65}\text{Mg}_{30}\text{Sn}_{1.10}$ (own type), $\text{La}_2\text{Mg}_{17}$ ($\text{Th}_2\text{Ni}_{17}$ -type), and $\text{CeMg}_{10.3}$ (own type) structures are related to the parental CaCu_5 -type structure (space group $P6/mmm$). As a result of tripling of the unit cell (1:5 stoichiometry) and replacing of a large atom (rare-earth element) with a pair of smaller atoms (transition element or other), we turn to the stoichiometry 2:17. By similar replacing, we can obtain other stoichiometry

such as 2:7, 5:19, 3:22, 3:29, etc. Insertion of additional atoms causes the formation of $\text{CeMg}_{10.3}$ and $\text{La}_{3.65}\text{Mg}_{30}\text{Sn}_{1.10}$ structures. The differences between these types of structures can be observed during the analysis of atomic networks that form magnesium atoms (Figure 3).

Table 3. Distribution of atoms in the Wyckoff sites for the $\text{La}_2\text{Mg}_{17}$, $\text{La}_{3.65}\text{Mg}_{30}\text{Sn}_{1.10}$, and $\text{Ce}_{1.71}\text{Mg}_{17.58}$ structures.

Wyckoff sites	$\text{La}_2\text{Mg}_{17}$		$\text{La}_{3.65}\text{Mg}_{30}\text{Sn}_{1.10}$		$\text{Ce}_{1.71}\text{Mg}_{17.58}$	
	Atoms	SOF	Atoms	SOF	Atoms	SOF
12	Mg	1.000	Mg	1.000	Mg	1.000
12j	Mg	1.000	Mg	1.000	Mg	1.000
6g	Mg	1.000	Mg	1.000	Mg	1.000
4f	Mg	1.000	Sn	0.217	Mg	0.985
4e	-	-	Sn	0.040	Mg	0.305
2d	-	-	Sn	0.032	Ce	0.015
2c	La	1.000	La	1.000	Ce	1.000
2b	La	1.000	La	0.826	Ce	0.695

**Figure 2.** Unit cell and coordination polyhedra of atoms for $\text{La}_{3.65}\text{Mg}_{30}\text{Sn}_{1.10}$.**Figure 3.** Magnesium atomic nets in the $\text{La}_{3.65}\text{Mg}_{30}\text{Sn}_{1.10}$, $\text{La}_2\text{Mg}_{17}$, and $\text{CeMg}_{10.3}$ related structures.

3.2. Powder XRD and EDX studies of $\text{La}_2\text{Mg}_{17-x}\text{M}_x$ alloy

The synthesized samples with the compositions $\text{La}_{10.5}\text{Mg}_{89.5}$, $\text{La}_{10.5}\text{Mg}_{85.5}\text{Sn}_4$, $\text{La}_{10.5}\text{Mg}_{85.5}\text{Sb}_4$ and $\text{La}_{10.5}\text{Mg}_{85.5}\text{Ni}_4$ were ingots of silver color and metallic luster and stable in air at room temperature. X-ray analysis showed the formation 2:17-phase (binary or ternary phases, ordered model) and small amounts of the other phases. The composition of this phase from EDX-analysis is $\text{La}_{11.2(5)}\text{Mg}_{88.8(9)}$ (Figure 4a). In binary alloy, the trace amount of LaMg_3 (structure type BiF_3 ,

space group $Fm-3m$, $a = 7.4807(5) \text{ \AA}$, $V = 418.63(8) \text{ \AA}^3$) was observed. The cubic phase (LaMg_3) did not show the corrosion stability in the electrolyte and after hydrogenation we observed traces of La_2O_3 .

Ni-contained alloys (from EDX-analysis $\text{La}_{10.3(4)}\text{Mg}_{85.3(7)}\text{Ni}_{4.4(7)}$) besides the main solid solution phase with nominal composition $\text{La}_2\text{Mg}_{16.2}\text{Ni}_{0.8}$ (Figure 4b) contained also the phase with high content of Mg (LaMg_{-12} , composition from EDX-analysis is $\text{La}_{8.2(7)}\text{Mg}_{90.6(9)}\text{Ni}_{1.2(9)}$).

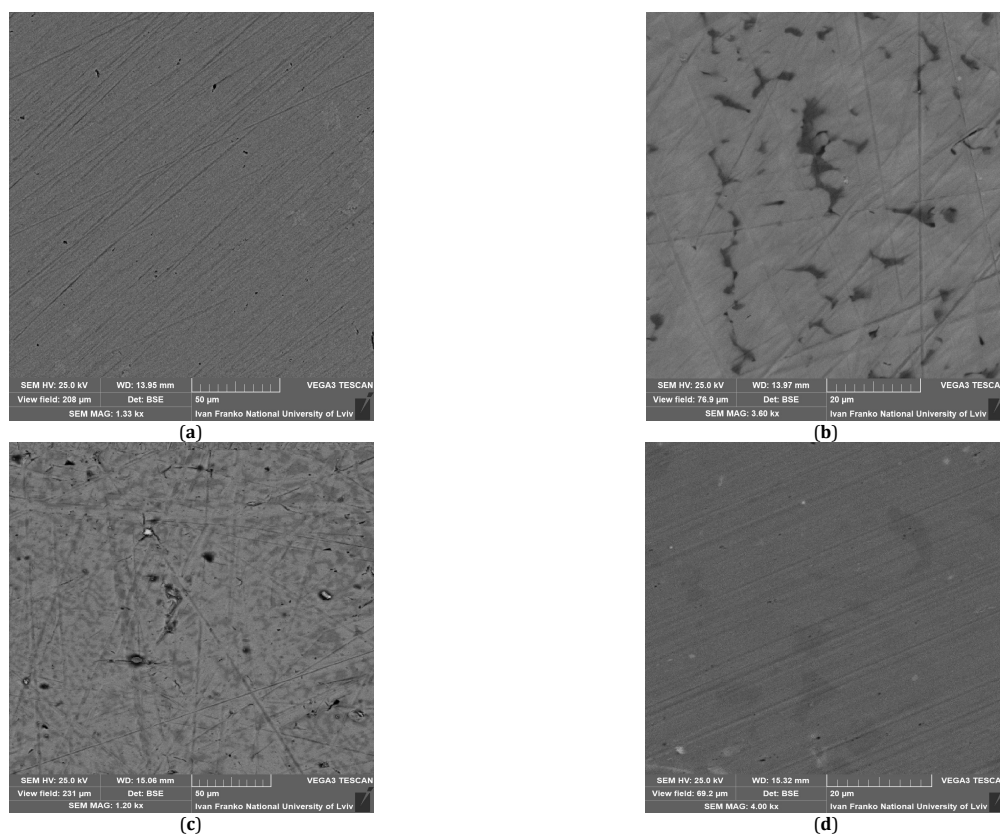


Figure 4. SEM-images (BSE-mode) of $\text{La}_{10.5}\text{Mg}_{89.5}$ (a), $\text{La}_{10.5}\text{Mg}_{85.5}\text{Ni}_4$ (b), $\text{La}_{10.5}\text{Mg}_{85.5}\text{Sn}_4$ (c) and $\text{La}_{10.5}\text{Mg}_{85.5}\text{Sb}_4$ (d).

Authors [25] also confirmed that the solubility of Ni in the 2:17-phase does not exceed 4-5 at. %. Authors [26] also were interested in electrochemical hydrogenation alloys of La-Mg-Ni system.

Tin-contained alloy contained the main phase $\text{La}_2\text{Mg}_{16.2}\text{Sn}_{0.8}$ (main phase, from EDX-analysis $\text{La}_{10.6(5)}\text{Mg}_{85.7(8)}\text{Sn}_{3.7(9)}$) and trace amount of ~Mg (dark phase, see Figure 4c, $\text{La}_{1.8(7)}\text{Mg}_{98.0(6)}\text{Sn}_{0.2(6)}$) and cubic $\text{LaMg}_{3-x}\text{Sn}_x$ (light points, $\text{La}_{24.3(5)}\text{Mg}_{73.4(6)}\text{Sn}_{2.3(7)}$). Similar content of phases is presented for Sb-contained alloy. Predicted solid solution $\text{La}_2\text{Mg}_{16.2}\text{Sb}_{0.8}$ (main phase, see Figure 4d) was with the composition $\text{La}_{11.1(5)}\text{Mg}_{84.2(8)}\text{Sb}_{4.7(6)}$. Trace amounts of Mg ($\text{La}_{2.2(6)}\text{Mg}_{95.9(8)}\text{Sb}_{1.9(8)}$) and cubic $\text{LaMg}_{3-x}\text{Sb}_x$ ($\text{La}_{24.8(5)}\text{Mg}_{72.2(7)}\text{Sb}_{3.0(7)}$, $a = 7.4639(8) \text{ \AA}$, $V = 415.8(1) \text{ \AA}^3$) phase were observed.

3.3. Electrochemical hydrogenation of $\text{La}_2\text{Mg}_{17-x}\text{M}_x$

All samples before and after electrochemical processes were examined by X-ray powder diffraction (diffractometer DRON-2.0M, Fe $K\alpha$ -radiation), X-ray fluorescent spectroscopy and EDX-analysis. Spectral analysis (Figure 5) confirmed the changes in electrode composition occurred as a result of hydrogenation. The main reason for it was the etching of surface and the forming of oxides of La and Sn on the surface that is associated with interaction of the electrode surface with an electrolyte, and this reaction affects the discharge capacity. The grain size decreased by hydrogenation, the surface of electrode grains became more porous and the morphology of the grain surface was changed. Also, the composition of the grains was shifted in the direction of reducing the lanthanum content.

Electrochemical hydrogenation was carried out in two-electrode Swagelok-type cells at galvanostatic mode (2 mA/cm²) to 3 H/f.u. For the binary and Sn-containing electrodes, we observed the formation and evolution of

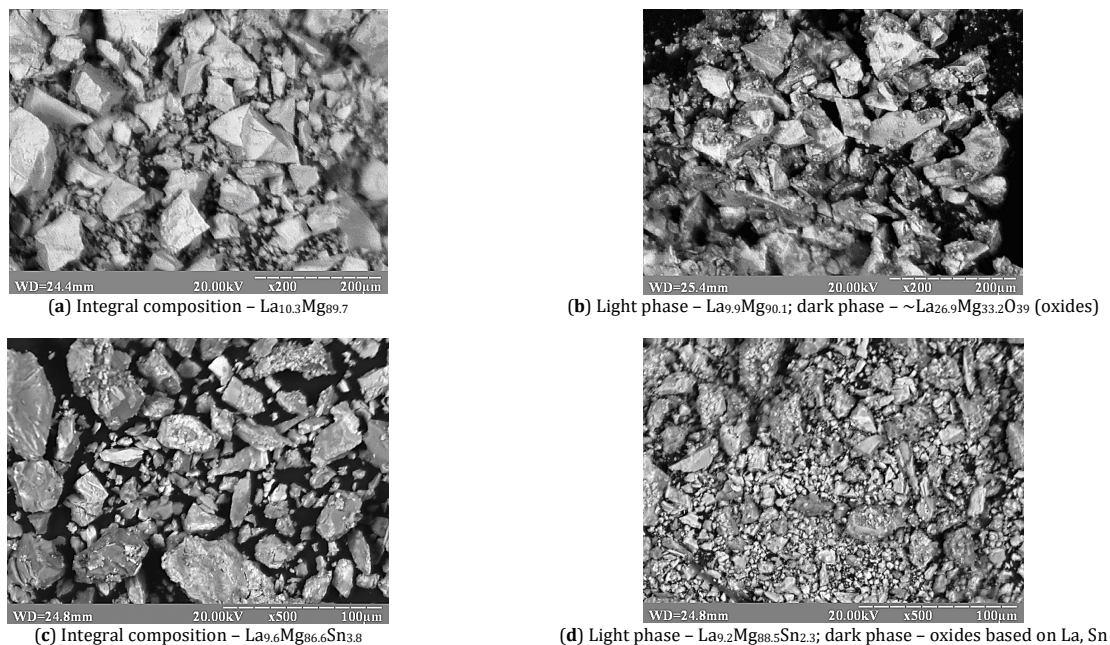
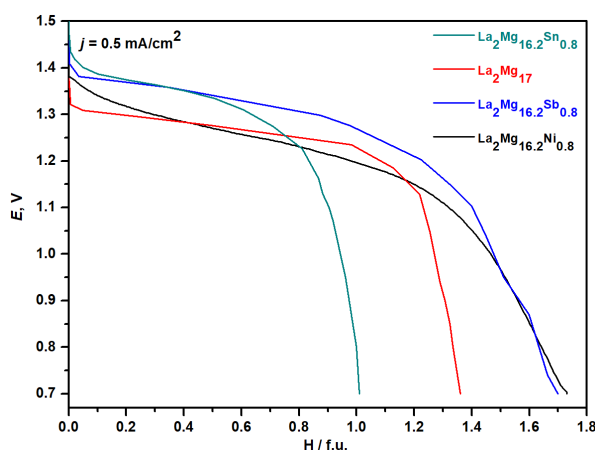
molecular hydrogen that correlates well with the discharge curves. In our opinion by gas hydrogenation we can obtain the hydrides with high H-content because high temperature and high pressure activates more grains. At the beginning of hydrogenation H-atoms occupy the octahedral voids with the position 6h forming the coordination polyhedra from two large and four small atoms (La_2Mg_4). Similar octahedral coordination of hydrogen atoms can be observed in the CaCu_5 -type structure. When the H-content is larger than 3 H/f.u., the tetrahedral composition 12i are occupied by hydrogen [27]. We think that H-atoms can occupy the tetrahedral positions of $\text{La}_2\text{Mg}_{17-x}\text{M}_x$ only by at high pressure or other extreme conditions. At experimental conditions we did not observe any evidences of structure decomposition after dehydrogenation.

Smaller amount of hydrogen (rectilinearly depends on the discharge time) was observed during dehydrogenation for $\text{La}_2\text{Mg}_{17}$ (1.36 H/f.u.) and $\text{La}_2\text{Mg}_{16.2}\text{Sn}_{0.8}$ (1.01 H/f.u.); in this case gas evolution took place as a side effect. Reversible content of hydrogen for the electrode on the basis of $\text{La}_2\text{Mg}_{16.2}\text{Sb}_{0.8}$ is 1.70 H/f.u. and for $\text{La}_2\text{Mg}_{16.2}\text{Ni}_{0.8}$ is 1.73 H/f.u. (Figure 6). After 50 cycles of electrochemical hydrogenation/dehydrogenation, the capacity of the battery prototype somewhat declined. It depends on the partial amorphization of the material and etching of the surface. While the electrochemical properties of the electrode materials depend on the corrosion stability of the alloys in the electrolyte solution (6 M KOH). In our previous works [5-7], doping $\text{Tb}_2\text{Ni}_{17}$ -based electrodes by s-elements (Li, Mg) and Sb led to the increasing of the corrosion stability and hydrogen sorption ability.

Nominal discharge voltage for the batteries with $\text{La}_2\text{Mg}_{17-x}\text{M}_x$ electrodes is bigger than in commercial batteries with AB_5 or AB_2 electrodes and is ~1.25-1.30 V. For example, the batteries based on AB_5 - and A_2B_{17} -electrodes with high Ni-content demonstrated the nominal discharge voltage in the range of 1.10-1.20 V.

Table 4. Unit cell parameters for 2:17 phases before hydrogenation (initial) and after hydrogenation (hydride of inclusion).

Phase / hydride	<i>a</i> , Å	<i>c</i> , Å	<i>V</i> , Å ³	$\Delta V/V$, %
La ₂ Mg ₁₇	10.339(1)	10.259(1)	949.7(2)	0.96
La ₂ Mg ₁₇ H _x	10.365(1)	10.303(2)	958.8(2)	
La ₂ Mg _{16.2} Sn _{0.8}	10.3478(6)	10.2728(7)	952.6(1)	0.45
La ₂ Mg _{16.2} Sn _{0.8} H _x	10.3629(8)	10.2888(9)	956.9(1)	
La ₂ Mg _{16.2} Sb _{0.8}	10.343(1)	10.222(1)	947.0(2)	1.18
La ₂ Mg _{16.2} Sb _{0.8} H _x	10.392(4)	10.245(4)	958.2(6)	
La ₂ Mg _{16.2} Ni _{0.8}	10.329(2)	10.236(2)	945.8(3)	1.43
La ₂ Mg _{16.2} Ni _{0.8} H _x	10.381(3)	10.279(4)	959.3(6)	

**Figure 5.** SEM-images of electrodes on the basis of La_{10.5}Mg_{89.5} and La_{10.5}Mg_{85.5}Sn₄ before (a), (c), and after (b), (d) 50 cycles of electrochemical hydrogenation.**Figure 6.** Selected discharge curves (30-th cycle) for the Ni-MH prototype batteries with La₂Mg_{17-x}M_x (*M* = Sn, Sb, Ni) as negative electrodes.

Changes in unit cell parameters of the solid solutions after electrochemical hydrogenation are presented in Table 4. For all samples after hydrogenation, we observed the increasing of the unit cell volume. As one can see, the unit cell parameters of the studied phases correlate well with the atomic radius of the alloying components ($r_{\text{Mg}} = 1.60 \text{ \AA}$, $r_{\text{Ni}} = 1.24 \text{ \AA}$, $r_{\text{Sn}} = 1.62 \text{ \AA}$, $r_{\text{Sb}} = 1.59 \text{ \AA}$).

4. Conclusion

Crystal structure of the solid solution La₂Mg_{17-x}Sn_x was determined by single crystal X-ray diffraction on the sample with the stoichiometry La_{3.65}Mg₃₀Sn_{1.10}. The phase crystallizes

in the hexagonal symmetry with the space group *P6₃/mmc* and is related to the structure of Th₂Ni₁₇ (ordered) and CeMg_{10.3} (disordered). The structure of La_{3.65}Mg₃₀Sn_{1.10} is strongly disordered and characterized by the split of some positions. Therefore, in the average structure, two subcells (A and B) can be selected, with the fraction ratio of subcell A to subcell B as 4:1. The A subcell has a composition La₄Mg₃₀Sn_{0.86} and B subcell has a composition La₂Mg₃₀Sn_{0.24}. The solubility of tin in the binary La₂Mg₁₇ intermetallic compound, studied by powder XRD and EDX-analysis, reaches 4 at. %. Solubility of Ni and Sb in the La₂Mg₁₇ compound is similar. The unit cell parameters of the solid solution La₂Mg_{17-x}M_x (*M* = Ni, Sn, Sb) correlate well with the atomic radii of doping components. As the electrode

materials studied, the alloys demonstrate the increasing of capacity in the line $\text{La}_2\text{Mg}_{16.2}\text{Sn}_{0.8}$ (1.01 H/f.u.) < $\text{La}_2\text{Mg}_{17}$ (1.36 H/f.u.) < $\text{La}_2\text{Mg}_{16.2}\text{Sb}_{0.8}$ (1.70 H/f.u.) < $\text{La}_2\text{Mg}_{16.2}\text{Ni}_{0.8}$ (1.73 H/f.u.) at 30-th cycle of charge/discharge. After 50 cycles of electrochemical measurements, the small shifting of electrode composition, changing of the morphology and grain size were observed.

Supporting information

CCDC-2059085 contains the supplementary crystallographic data for this paper. These data can be obtained free of charge via <https://www.ccdc.cam.ac.uk/structures/>, or by emailing data_request@ccdc.cam.ac.uk, or by contacting The Cambridge Crystallographic Data Centre, 12 Union Road, Cambridge CB2 1EZ, UK; fax: +44(0)1223-336033 and may be obtained from FIZ Karlsruhe, 76344 Eggenstein-Leopoldshafen, Germany (fax: (+49)7247-808-666; e-mail: crysdata@fiz-karlsruhe.de).

Disclosure statement

Conflict of interests: The authors declare that they have no conflict of interest.

Author contributions: All authors contributed equally to this work.

Ethical approval: All ethical guidelines have been adhered.

Sample availability: Samples of the compounds are available from the author.

ORCID

Vasyl Kordan

 <https://orcid.org/0000-0001-8319-5816>

Vitalii Nytko

 <https://orcid.org/0000-0002-6090-9473>

Ivan Tarasiuk

 <https://orcid.org/0000-0002-6590-5527>

Oksana Zelinska

 <https://orcid.org/0000-0002-2931-9870>

Volodymyr Pavlyuk

 <https://orcid.org/0000-0003-1893-2706>

References

- [1]. Besenhard, J. O. *Handbook of Battery Materials*; Besenhard, J. O., Ed.; Wiley-Vch, 1999.
- [2]. Balińska, A.; Kordan, V.; Misztal, R.; Pavlyuk, V. *J. Solid State Electrochem.* **2015**, *19* (8), 2481–2490.
- [3]. Kowalczyk, G.; Kordan, V.; Stetskiv, A.; Pavlyuk, V. *Intermetallics (Barking)* **2016**, *70*, 53–60.
- [4]. Kordan, V.; Zelinska, O.; Tarasiuk, I.; Zelinska, O.; Pavlyuk, V. *Chem. Met. Alloys* **2014**, *7*(1/2), 106–111. <http://www.chemetal-journal.org/ejournal14/CMA0282.pdf> (accessed Apr 6, 2021).
- [5]. Kordan, V.; Zelinska, O.; Pavlyuk, V.; Oshchapovsky, I.; Serkiz, R. *Chem. Met. Alloys* **2016**, *9*(1/2), 84–91. <https://chemetal-journal.org/ejournal18/CMA0327.pdf> (accessed Apr 6, 2021).
- [6]. Pavlyuk, V.; Ciesielski, W.; Pavlyuk, N.; Kulawik, D.; Szyrej, M.; Rozdzyńska-Kielbik, B.; Kordan, V. *Ionics (Kiel)* **2019**, *25* (6), 2701–2709.
- [7]. Pavlyuk, V.; Ciesielski, W.; Pavlyuk, N.; Kulawik, D.; Kowalczyk, G.; Balińska, A.; Szyrej, M.; Rozdzyńska-Kielbik, B.; Foleńtarska, A.; Kordan, V. *Mater. Chem. Phys.* **2019**, *223*, 503–511.
- [8]. Kordan, V.; Nytko, V.; Kowalczyk, G.; Balińska, A.; Zelinska, O.; Serkiz, R.; Pavlyuk, V. *Chem. Met. Alloys.* **2017**, *10*(1/2), 61–68. <https://chemetal-journal.org/ejournal21/CMA0355.pdf> (accessed Apr 6, 2021).
- [9]. Yartys, V.; Noreus, D.; Latroche, M. *Appl. Phys. A Mater. Sci. Process.* **2016**, *122* (1), 43–54.
- [10]. Li, P.; Zhang, J.; Zhai, F.; Ma, G.; Xu, L.; Qu, X. *J. Rare Earths* **2015**, *33* (4), 417–424.
- [11]. Hadjixenophontos, E.; Roussel, M.; Sato, T.; Weigel, A.; Stender, P.; Orimo, S.-I.; Schmitz, G. *Int. J. Hydrogen Energy* **2017**, *42* (35), 22411–22416.
- [12]. Zhou, W.; Ma, Z.; Wu, C.; Zhu, D.; Huang, L.; Chen, Y. *Int. J. Hydrogen Energy* **2016**, *41* (3), 1801–1810.
- [13]. Liu, Y.; Yuan, H.; Guo, M.; Jiang, L. *Int. J. Hydrogen Energy* **2019**, *44* (39), 22064–22073.
- [14]. Liu, J.; Zhu, S.; Cheng, H.; Zheng, Z.; Zhu, Z.; Yan, K.; Han, S. *J. Alloys Compd.* **2019**, *777*, 1087–1097.
- [15]. Wang, L.; Zhang, X.; Zhou, S.; Xu, J.; Yan, H.; Luo, Q.; Li, Q. *Int. J. Hydrogen Energy* **2020**, *45* (33), 16677–16689.
- [16]. Dutta, K.; Srivastava, O. N. *J. Mater. Sci.* **1993**, *28* (13), 3457–3462.
- [17]. De Negri, S.; Solokha, P.; Minetti, R.; Skrobańska, M.; Saccone, A. *J. Solid State Chem.* **2017**, *248*, 32–39.
- [18]. King, G.; Schwarzenbach, D. L. *Xtal 3. 7 System*; University of Western Australia, 2000.
- [19]. Kraus, W.; Nolze G. *Powder Cell for Windows*, Berlin, 1999.
- [20]. MTech Lab - Measuring technologies, <http://chem.lnu.edu.ua/mtech/mtech.htm> (accessed Apr 6, 2021).
- [21]. SADABS, Bruker AXS Inc., Wisconsin, Madison, USA, 2009.
- [22]. Sheldrick, G. M. *Acta Crystallogr. A* **2008**, *64* (1), 112–122.
- [23]. Sheldrick, G. M. *Acta Crystallogr. C Struct. Chem.* **2015**, *71* (1), 3–8.
- [24]. Freccero, R.; De Negri, S.; Saccone, A.; Solokha, P. *Dalton Trans.* **2020**, *49* (34), 12056–12067.
- [25]. De Negri, S.; Giovannini, M.; Saccone, A. *J. Alloys Compd.* **2005**, *397* (1–2), 126–134.
- [26]. Balcerzak, M.; Nowak, M.; Jurczyk, M. *Int. J. Hydrogen Energy* **2017**, *42* (2), 1436–1443.
- [27]. Isnard, O.; Miraglia, S.; Soubeyroux, J. L.; Fruchart, D.; Stergiou, A. *J. Less-Common Met.* **1990**, *162* (2), 273–284.



Copyright © 2021 by Authors. This work is published and licensed by Atlanta Publishing House LLC, Atlanta, GA, USA. The full terms of this license are available at <http://www.eurjchem.com/index.php/eurjchem/pages/view/terms> and incorporate the Creative Commons Attribution-Non Commercial (CC BY NC) (International, v4.0) License (<http://creativecommons.org/licenses/by-nc/4.0>). By accessing the work, you hereby accept the Terms. This is an open access article distributed under the terms and conditions of the CC BY NC License, which permits unrestricted non-commercial use, distribution, and reproduction in any medium, provided the original work is properly cited without any further permission from Atlanta Publishing House LLC (European Journal of Chemistry). No use, distribution or reproduction is permitted which does not comply with these terms. Permissions for commercial use of this work beyond the scope of the License (<http://www.eurjchem.com/index.php/eurjchem/pages/view/terms>) are administered by Atlanta Publishing House LLC (European Journal of Chemistry).